

Article

Electrochemical Synthesis-Dependent Photoelectrochemical Properties of Tungsten Oxide Powders

Anastasia Tsarenko ¹, Mikhail Gorshenkov ², Aleksey Yatsenko ¹, Denis Zhigunov ³ , Vera Butova ⁴, Vasily Kaichev ⁵  and Anna Ulyankina ^{1,*} 

¹ Research Institute "Nanotechnologies and New Materials", Platov South-Russian State Polytechnic University (NPI), 346428 Novocherkassk, Russia; tsarenkoanasteisha@yandex.ru (A.T.); alexyats-npi@yandex.ru (A.Y.)

² Department of Physical Materials Science, National University of Science & Technology (MISIS), 119049 Moscow, Russia; mvgorshenkov@gmail.com

³ Center for Photonics and Quantum Materials, Skolkovo Institute of Science and Technology, 121205 Moscow, Russia; dmzhigunov@physics.msu.ru

⁴ The Smart Materials Research Institute, Southern Federal University, 344090 Rostov-on-Don, Russia; butovav86@gmail.com

⁵ Department of Investigation of Catalysts, Boreskov Institute of Catalysis, 630090 Novosibirsk, Russia; vvk@catalysis.ru

* Correspondence: anya-barbashova@yandex.ru

Abstract: A rapid, facile, and environmentally benign strategy to electrochemical oxidation of metallic tungsten under pulse alternating current in an aqueous electrolyte solution was reported. Particle size, morphology, and electronic structure of the obtained WO₃ nanopowders showed strong dependence on electrolyte composition (nitric, sulfuric, and oxalic acid). The use of oxalic acid as an electrolyte provides a gram-scale synthesis of WO₃ nanopowders with tungsten electrochemical oxidation rate of up to 0.31 g·cm⁻²·h⁻¹ that is much higher compared to the strong acids. The materials were examined as photoanodes in photoelectrochemical reforming of organic substances under solar light. WO₃ synthesized in oxalic acid is shown to exhibit excellent activity towards the photoelectrochemical reforming of glucose and ethylene glycol, with photocurrents that are nearly equal to those achieved in the presence of simple alcohol such as ethanol. This work demonstrates the promise of pulse alternating current electrosynthesis in oxalic acid as an efficient and sustainable method to produce WO₃ nanopowders for photoelectrochemical applications.

Keywords: tungsten oxide; electrochemical synthesis; pulse alternating current; photoelectrochemical reforming



Citation: Tsarenko, A.; Gorshenkov, M.; Yatsenko, A.; Zhigunov, D.; Butova, V.; Kaichev, V.; Ulyankina, A. Electrochemical Synthesis-Dependent Photoelectrochemical Properties of Tungsten Oxide Powders. *ChemEngineering* **2022**, *6*, 31. <https://doi.org/10.3390/chemengineering6020031>

Academic Editor: Alirio E. Rodrigues

Received: 9 March 2022

Accepted: 13 April 2022

Published: 15 April 2022

Publisher's Note: MDPI stays neutral with regard to jurisdictional claims in published maps and institutional affiliations.



Copyright: © 2022 by the authors. Licensee MDPI, Basel, Switzerland. This article is an open access article distributed under the terms and conditions of the Creative Commons Attribution (CC BY) license (<https://creativecommons.org/licenses/by/4.0/>).

1. Introduction

Photoelectrochemical (PEC) water splitting provides a great opportunity to produce environmentally friendly H₂ fuel by direct conversion of solar energy to establish a CO₂ zero emission society. The efficiency of PEC water splitting reaction, as a matter of fact, is quite low due to the recombination of the photogenerated charge carriers [1]. The enhanced efficiency of hydrogen evolution can be reached by introducing various sacrificial electron donor reagents in water for the irreversible reaction with h⁺ from photogenerated electron-hole pairs [2].

The most used sacrificial agents for photo- and photoelectrochemical reforming of organic materials are simple alcohols, such as methanol, ethanol, etc. [3]. However, enormous amounts of waste containing glycerol and ethylene glycol are generated by industries, resulting in a serious environmental problem [4]. Moreover, involvement of biomass-derived compounds offers a feasible approach for both sustainable H₂ production and biomass valorization with renewable solar energy [5]. Lately, a PEC cell functioning in the presence of an organic sacrificial agent was referenced as a photoactivated fuel cell (PFC) [6]. PFC

consists of a semiconductor photoanode that performs an organic oxidation reaction under illumination and a cathode where H_2 may be formed as a result of water or H^+ reduction. Although all PFC components can affect its performance, the nature of semiconductor electrode has an essential role in its functioning.

Up until now, a wide range of semiconductors have been explored as photoanodic materials, including metal oxides, nitrides, and sulfides. Most of the PEC studies have been mainly focused on metal oxides based photoanodes due to their low cost and environmental friendliness [7].

Tungsten oxide (WO_3) is considered as one of the most earth-abundant and promising candidates for the photoanode in PEC [8,9]. On the one hand, its relatively high absorption of solar light (up to 480 nm) due to a small band gap of 2.5–2.8 eV and its deep valence band position perfectly match the thermodynamic energy requirements needed to drive water/organics oxidation. On the other hand, WO_3 exhibits high stability in harsh acidic environment, a moderate hole diffusion length (~150 nm) compared to other common semiconductor oxides, and better electron transport ($12 \text{ cm}^2 \cdot \text{V}^{-1} \cdot \text{s}^{-1}$) compared to TiO_2 ($0.3 \text{ cm}^2 \cdot \text{V}^{-1} \cdot \text{s}^{-1}$) [10]. The photoelectrochemical efficiency of WO_3 is determined by its structure-dependent properties. The most widely used approach for the fabrication of diverse WO_3 nanostructures is wet-chemical synthesis. However, there is still a great challenge to control over their properties using a facile and green method [11]. Most of the employed techniques are complex, and thus less suitable for industrial applications. Recently, electrochemical synthesis of nanosized metal oxides has been considered as a sustainable and economically attractive method to produce highly efficient catalysts [12,13]. Electrosynthesis demonstrates many advantages compared with other physical and chemical methods such as low temperature, aqueous media, simple operation, etc. The most works have been focused on the anodization of tungsten as a valve metal to fabricate WO_3 thin films on the metal substrate [14,15]. However, there is a sense to develop electrochemical synthesis of WO_3 powders with controllable characteristics for various applications. There have been several reports about the production of WO_3 powder particles by an electrochemical route. Particularly, the preparation of $WO_3 \cdot 2H_2O$ nanoplatelets by anodization of tungsten under breakdown conditions was described elsewhere [16]. However, a study on the photoelectrochemical properties of WO_3 powders prepared in different electrolytes under pulse alternating current (PAC) is not reported in the literature yet. In our previous works, the effect of PAC synthesis conditions (current density and electrolytic media) on structural and functional properties of semiconductor materials such as ZnO [17] and CuO_x [18] was reported.

In the current study we demonstrate that WO_3 nanopowders can be successfully synthesized by safe, fast, and scalable electrochemical method using pulse alternating current. The influence of electrolytic media (oxalic, sulfuric, and nitric acid) on structural characteristics and electronic structure as well as photoelectrochemical properties of WO_3 nanoparticles was studied. These results highlight a novel electrochemical strategy to fabricate WO_3 powders for photoelectrochemical applications.

2. Materials and Methods

2.1. Preparation of WO_3 Powders

WO_3 nanopowders were synthesized by electrochemical method under pulse alternating current using different aqueous electrolyte solutions such as oxalic acid (0.5 M), sulfuric acid (0.5 M), and nitric acid (0.5 M). Electrochemical synthesis was executed at a current density ratio ($j_a:j_c$) of 3:3 $A \cdot \text{cm}^{-2}$ for 1 h with tungsten (W) foils (0.1 mm thickness) as the anode and cathode at a constant stirring speed of 200 rpm. The constant temperature of electrolyte was maintained using a cooling jacket. After synthesis the obtained powders were separated, washed with ethanol until neutral pH was achieved and dried. The as-prepared nanopowders were annealed in air using a muffle furnace at 500 °C for 3 h.

2.2. Characterization of WO₃ Powders

Morphologies of the powders obtained during tungsten electrochemical oxidation under pulse alternating current were characterized using a scanning electron microscope (SEM), JEOL, with an acceleration voltage of 30 kV and a JEOL JEM-2100 transmission electron microscope (TEM) operating at 200 kV. X-ray diffraction (XRD) measurements were performed to confirm the crystal structure using an ARL X'TRA X-ray diffractometer (Thermo Fisher Scientific Inc., Waltham, MA, USA) with Cu K α radiation ($\lambda = 1.5406 \text{ \AA}$). The Rietveld refinement of the XRD data has been done using the JAVA based software namely Materials Analysis Using Diffraction (MAUD). Raman spectra were recorded on a DRX Raman microscope (Thermo Fisher Scientific Inc.) using a 532 nm laser for excitation. UV–vis reflectance spectra (UV-vis DRS) were recorded on a UV-2600 UV–visible spectrophotometer (Shimadzu) with an integrating sphere attachment. BET analysis was performed using a Micromeritics ASAP 2020 Physisorption BET instrument. Surface elemental composition and electronic valence band spectra were examined using X-ray photoelectron spectroscopy (XPS). The spectra were recorded on an X-ray photoelectron spectrometer (SPECS Surface Nano Analysis GmbH) using non-monochromatic Al K α radiation ($h\nu = 1486.6 \text{ eV}$). To analyze the presence of impurities, survey spectra were taken using the pass energy of 50 eV. The valence band, C1s, O1s, and W4f spectra, were obtained using the pass energy of 20 eV. The CasaXPS software was used to analyze the XPS spectra. Charge correction was performed by setting the C1s peak at 284.8 eV from adventitious hydrocarbon.

2.3. Photoelectrochemical Measurements

Fabrication of WO₃ photoanode was performed through a drop-casting method. First, 50 mg of the WO₃ nanopowder dispersed and ultrasonicated for 30 min in 2 mL of isopropanol was dropped onto a fluorine-doped tin oxide (FTO) glass substrate. Prior to drop casting, the FTO substrate was cleaned and ultrasonicated with acetone and then water. The fabricated WO₃ film was then dried at room temperature, annealed in air at 500 °C for 30 min, and used as the working electrode.

Photoelectrochemical properties of the WO₃/FTO photoanode were studied in a three-electrode electrochemical cell equipped with a quartz window using a P-45X potentiostat-galvanostat system (Elins, Russia) where Ag/AgCl (in 3.5 M KCl) and platinum wire were used as the reference and counter electrodes, respectively. The geometrical surface area of WO₃/FTO photoanode was equal to 1.0 cm². The measurements were performed in 0.5 M aqueous H₂SO₄ solution as the electrolyte. The impact of various sacrificial reagents on the photoelectrochemical activity of WO₃ was studied using the aqueous electrolyte, which contained 0.5 M H₂SO₄ and 5 mM of glycerol, ethylene glycol, glucose, and ethanol. A solar simulator equipped with a 500 W Xenon lamp was employed as the light source (AM 1.5G). The simulated solar illumination was adjusted to 1 sun (100 mW·cm⁻²). Linear sweep voltammograms (LSV) were recorded from 0 to 1.6 V vs. Ag/AgCl at a fixed scan rate of 10 mV·s⁻¹ with chopping light. The photocurrent density-time transients were measured at 0.8 V vs. Ag/AgCl. Open circuit potential (OCP) of the prepared photoanodes was determined in the dark and light illumination. Applied bias photon-to-current efficiency (ABPE) was calculated using the following equation:

$$\text{ABPE (100\%)} = J \cdot \frac{1.23 - E_{RHE}}{P_{light}} \cdot 100\%$$

where J is the photocurrent density, E_{RHE} is the potential versus RHE, and P_{light} is the simulated solar light intensity.

The electrochemical impedance measurements were carried out with a three-electrode system in 0.5 M H₂SO₄ electrolyte under the same illumination conditions in the frequency range of 0.1 Hz–50 kHz. Electrochemically active surface area (ECSA) determination was performed at scan rates of 10–50 mV s⁻¹ in 0.5 M H₂SO₄.

3. Results and Discussion

3.1. Characterization of the Powders

To investigate the microstructural characteristics of the products obtained during tungsten electrochemical oxidation under pulse alternating current, electron microscopy was employed. Figure 1a–f show the SEM images of the powders formed in the presence of nitric ($\text{WO}_3\text{-NA}$), oxalic ($\text{WO}_3\text{-OA}$), and sulfuric ($\text{WO}_3\text{-SA}$) acids and annealed at 500 °C. It is evident that the electrolyte has a great influence on the morphology and size of the prepared powders. In the presence of HNO_3 , the product of W electrochemical oxidation is mainly composed of the large and well-formed plates with a length of 400–600 nm and thickness of 30–60 nm mixing with smaller nanoparticles with a side length of ~30 nm (Figure 1a,d). Similar morphology was obtained by authors [19] during W anodization at high temperature in strongly acidic electrolyte without the addition of complexing agent. Using H_2SO_4 as an electrolyte led to the disappearance of large plates (Figure 1b,e,h). The irregular nanoparticles (20–30 nm in size) are mainly present. However, a small number of particles with a length size of ~100 nm is still observed. The sample prepared in oxalic acid is consisted of the predominantly round-shaped particles with their side lengths distributed in the range of ~10–30 nm (Figure 1c,f,i). TEM, HRTEM, and the corresponding fast-Fourier-transform (FFT) images were demonstrated in Figure 1g–i.

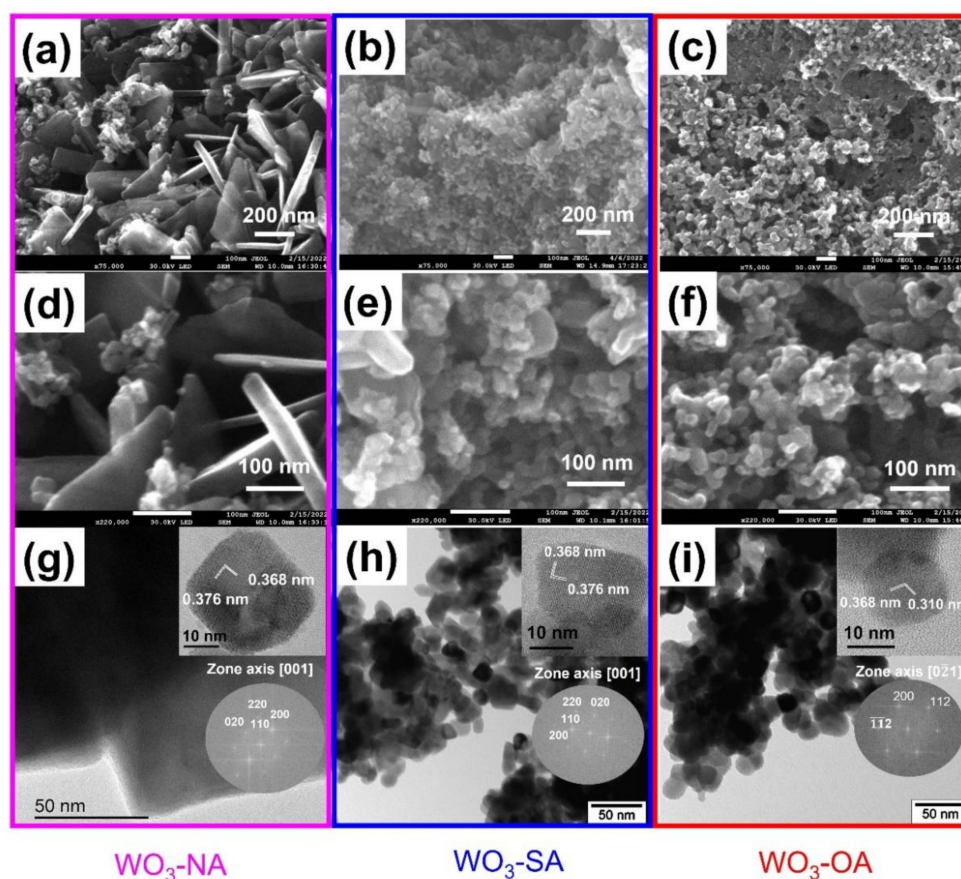


Figure 1. SEM (a–f), TEM (g–i), and corresponding HRTEM and FFT images (inset) of the products of tungsten electrochemical oxidation under pulse alternating current in nitric (a,d,g), sulfuric (b,e,h), and oxalic (c,f,i) acids.

For $\text{WO}_3\text{-NA}$ and $\text{WO}_3\text{-SA}$ samples, the measured lattice spacing of $d = 0.376$ nm and $d = 0.368$ nm can be assigned to the (020) and (200) crystal planes of the monoclinic WO_3 structure, respectively. For $\text{WO}_3\text{-OA}$, the lattice spacings of $d = 0.361$ nm and $d = 0.310$ nm can be assigned to the (200) and (112) planes of the monoclinic WO_3 , respectively. The

monoclinic phase was found to be the most stable and suitable for photoelectrochemical applications [20].

To examine the influence of electrolyte on the composition and crystalline structure of the products obtained during W electrochemical oxidation under pulse alternating current X-ray diffraction and Raman spectroscopy were used for additional characterization. Based on XRD results, the phase analysis of the obtained products is rather difficult due to non-Bragg scattering phenomena together with extremely broadened peaks. The overlapping of reflections is reported to be typical for such samples [21]. However, the XRD patterns of all the samples could be well fitted to the monoclinic WO_3 crystal phase with space group of $P 2_1/n$ (ICSD # 80056) [21] that is consistent with the HRTEM data. Figure 2a shows the experimental patterns obtained for the three samples, along with the simulated diffractograms using the MAUD software. The crystallographic parameters obtained for all samples from the Rietveld refinements are reported in Table S1. The fitting data demonstrate the variation of WO_3 lattice parameters that can be due to morphological changes of the prepared powders [22]. The average crystallite size of the particles calculated using XRD data according to Debye-Scherrer equation [23] was found to be 37.2, 18.6, and 13.3 nm for WO_3 -NA, WO_3 -SA, and WO_3 -OA, respectively.

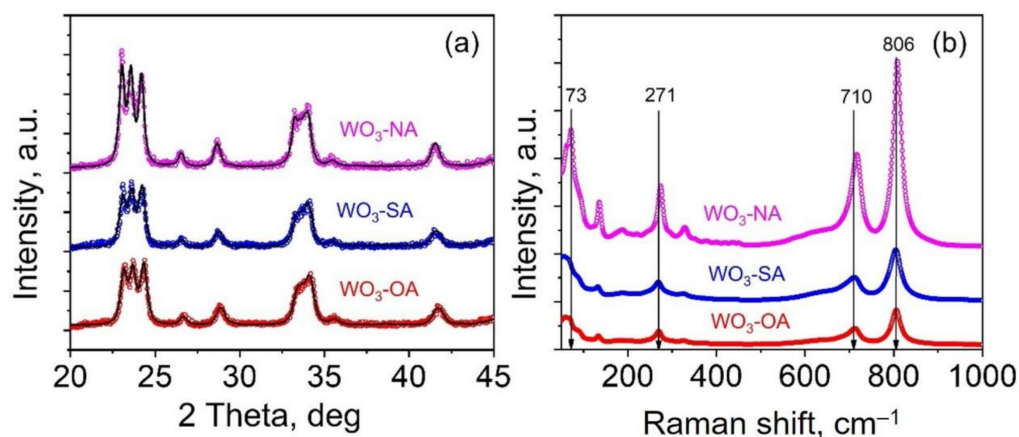


Figure 2. XRD patterns (a) and Raman spectra (b) of products obtained by electrochemical oxidation of tungsten under pulse alternating current using oxalic acid (WO_3 -OA), sulfuric acid (WO_3 -SA), and nitric acid (WO_3 -NA). The measured diffraction data are shown by circles, and the calculated are shown by solid lines in black.

Raman spectroscopy is an effective way to study subtle change in the crystal structure due to high sensitivity to the phase transition and the structure defects [24]. The Raman spectra (Figure 2b) of all samples exhibited vibrations in three regions at 900–600, 400–200, and below 200 cm^{-1} which corresponds to the W–O stretching, W–O deformation, and lattice modes of the monoclinic WO_3 crystal phase, respectively. All the Raman spectra have been fitted by Lorentzian components (Figure S1). The bands at 271, 710, and 806 cm^{-1} were identified as the three strongest modes of monoclinic tungsten oxide. The Raman bands at 271 and 327 cm^{-1} correspond to O–W–O bending modes. The two sharp peaks at 710 and 806 cm^{-1} both result from O– W^{6+} –O stretching modes in the WO_6 octahedral unit [25].

The significant increase in intensity of the O–W–O Raman vibrations of WO_3 -NA sample is most probably correlated with the degree of crystallinity and the particle size of the powders. The higher peak intensity reflects a considerable improvement in the structural order of the powders in terms of bond length and angle of the O–W–O bonding [26]. Some authors demonstrated that the weak and broad peaks in Raman spectra could be attributed to the local lattice imperfections, revealing the absence of partial O atoms in the WO_{3-x} structure [27]. Moreover, a blue shift of the peaks is evident when nitric acid is used for

the WO_3 synthesis that can be also due to the improved crystallinity of the material or the crystallite size effect [26,28].

The surface elemental compositions of the synthesized WO_3 nanopowders were studied by X-ray photoelectron spectroscopy. The data are shown in Figures S2 and S3. The XPS scan (Figure S2a) indicates the presence of W, O, and C as main elements in the WO_3 samples. The C1s spectra in Figure S2b can be deconvoluted into three peaks at 284.8, 286.3–286.5, and 288.8–288.9 eV, and are due to C-C/C-H, C-OH/C-O-C, and O=C-C bonds, respectively. For all tested samples, the W4f spectra was approximated well by two spin-orbital $W4f_{7/2}$ - $W4f_{5/2}$ doublets (Figure 3a). The main doublet with the $W4f_{7/2}$ binding energy of 35.5 eV corresponds to W^{6+} species and a less intense doublet with the $W4f_{7/2}$ binding energy of 33.8–33.9 eV can be probably ascribed to W^{5+} species [29,30]. The content of W^{5+} species in all samples calculated using the XPS data is 3–4%. The O1s peak can be approximated by three components (Figure 3b). The peak at the highest binding energy (530.2–530.4 eV) derives from the oxygen in the strong W-O bonds of WO_3 . The O1s peak at 531.5–531.7 eV corresponds to the oxygen from the surface hydroxyl groups. The O1s peak at 532.9–533.1 eV is assigned to the oxygen from water molecules physisorbed on the surface of oxide [29,31,32]. Furthermore, the nature of electrolytes used during synthesis exerts negligible influence on the chemical states of W and O. To determine the relative band edges of the WO_3 crystals, the valence band spectra were recorded and shown in Figure 3c. WO_3 synthesized in oxalic and sulfuric acids have a deeper VB maximum by 0.1 eV than WO_3 prepared in nitric acid, suggesting a stronger oxidation power of photoexcited VB holes in the former [20].

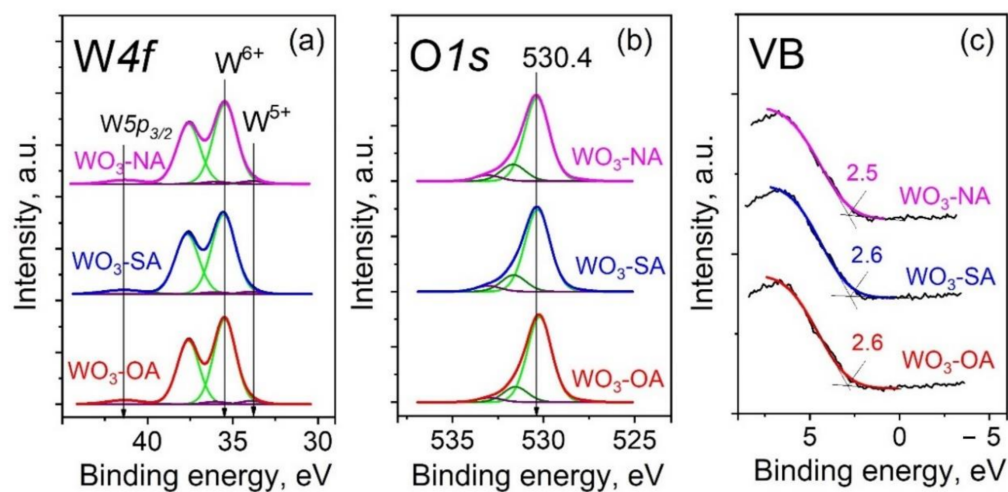


Figure 3. Deconvoluted high-resolution XPS spectra of W4f core level (a) and O1s core levels (b). XPS valence band edge plot of WO_3 prepared in different electrolytes (c).

Figure S3 shows the nitrogen adsorption–desorption isotherms of all samples prepared using different acidic electrolytes. According to the IUPAC classification, WO_3 nanoparticles exhibit type IV nitrogen physisorption isotherm with type H3 hysteresis loop, resulting from pore structures giving wedge-shaped or groove mesopores of 2–12 nm in diameter presumably formed by aggregates with plate-like nanoparticles [33]. The inset table in Figure S3 shows the corresponding SSA and pore volume values. It can be observed that SSA of WO_3 -SA and WO_3 -NA samples are quite similar (11.4 and 14.2 m^2/g , respectively). The reduction in surface area, which is probably due to a higher agglomeration effect, is more pronounced for WO_3 -OA (7.58 m^2/g).

The UV-vis diffuse reflectance spectra of the WO_3 samples are shown in Figure 4a. It is evident that WO_3 -OA sample exhibits enhanced visible light absorption in the range 460–800 nm compared to WO_3 -SA and WO_3 -NA. The more efficient harvesting of visible light is commonly ascribed to the possible modification in the crystal structure [34,35]. Generally, the photoactivity of the semiconductor materials is defined by the band gap

energy. The optical band gap (E_g) of the prepared materials was extrapolated via the Kubelka-Munk method and extracted from the plot of $(F(R) \times h\nu)^{1/2}$ versus $E (h\nu)$. The E_g values WO_3 -OA, WO_3 -SA, and WO_3 -NA were 2.53, 2.55, and 2.62 eV, respectively (Figure 4b). The band gap values are consistent with reported ones for monoclinic WO_3 synthesized using chemical routes [22,35]. The difference in band gap can originate from the different morphology and orientation of crystal facets. It was reported earlier that electronic band structure of WO_3 can be tuned by formation of crystals with different morphology, such as quasi-cubic and rectangular sheet [20].

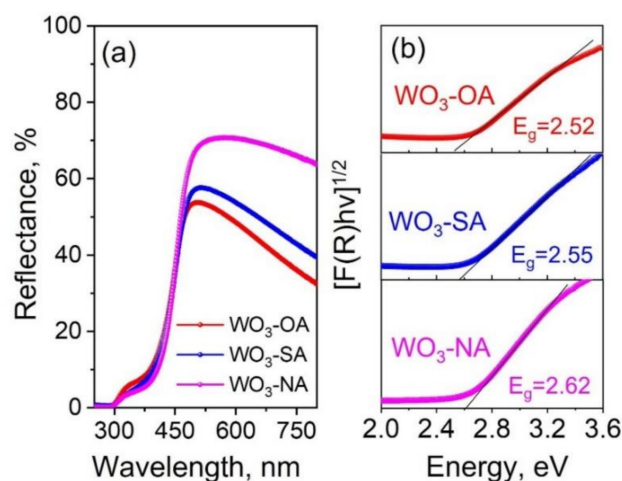
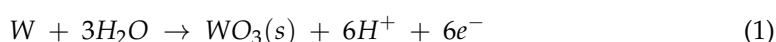


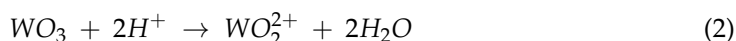
Figure 4. Diffuse reflectance (a) and band gap determination curves (b) of WO_3 prepared using different electrolytes.

3.2. Possible Formation Mechanism

The oxidation of W electrode during anodic pulse takes place indicating the fast formation of a compact isolating WO_3 layer according to the following reaction (1) [36]:

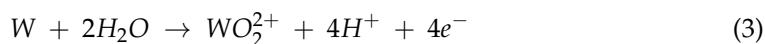


Although WO_3 is thermodynamically stable in acidic solutions, this layer can undergo electrical-field-induced dissolution (2) by the action of protons, resulting in WO_2^{2+} species formation.



Due to its great affinity to oxygen, tungsten forms a metal/metal oxide/metal ion irreversible system. The chemical nature of the oxide layer on the W substrate is generally influenced by pH, temperature, concentration, presence of complexing agents, etc.

At high pH, electrochemical dissolution of the tungsten substrate through the oxide is also possible according to the reaction (3):



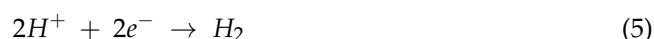
The highest electrochemical oxidation rate of tungsten (up to $0.31 \text{ g} \cdot \text{cm}^{-2} \cdot \text{h}^{-1}$) was observed in the oxalic acid solution compared to nitric and sulfuric acids (Figure S4). Moreover, an increase in the oxalic acid concentration resulted in a higher dissolution rate of the WO_3 layer. These results imply that OA promoted the active dissolution of the substrate via complexation, forming soluble complexes between oxalate and tungsten released to the electrolyte. The formation of WO_3 films by anodization through a dissolution-precipitation mechanism in the presence of citric acid as a complexing agent was previously shown [9].

Upon reaching supersaturation conditions, the soluble species WO_2^{2+} precipitates on the electrode surface [37].



The formation of orthorhombic tungsten oxide monohydrate ($WO_3 \cdot H_2O$ space group *Pmnb*, No. 62, $Z = 4$, $a = 5.2477 \text{ \AA}$, $b = 10.7851 \text{ \AA}$, $c = 5.1440 \text{ \AA}$) [38] as a product of *W* oxidation under pulse alternating current was confirmed by XRD for all used electrolytes (Figure S5). The electrolytic media influence the crystallinity of the as-prepared $WO_3 \cdot H_2O$. The lowest crystallinity confirmed by low and wide peaks in the XRD pattern was observed in the presence of oxalic acid. It can be explained by the decrease in the ordering effect in oxalic acid, which resulted in the formation of less compact structures [39].

During cathodic pulse, the hydrogen ions are reduced to hydrogen gas molecules:



Hydrogen bubbles, after reaching some critical size, detach from the electrode and move to the electrolyte/air interface and promote the removal of the already formed $WO_3 \cdot H_2O$ particles from the electrode surface [40]. Thereby, application of pulse alternating current (sequence of anodic and cathodic pulses with pauses between them) results in formation of microporous multi-layer film of $WO_3 \cdot H_2O$ which has micro-scale wicking channels (Figure S6). No WO_3 powder is observed in the electrolyte solution when an anodic pulse current of the same density is used.

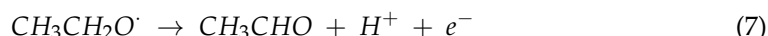
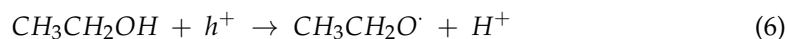
3.3. Photoelectrochemical Performance

PEC properties of WO_3 nanoparticles synthesized in different electrolytes were evaluated by various electrochemical techniques in an aqueous electrolyte solution (H_2SO_4 , 0.5 M). LSV curves under chopped illumination were recorded for all samples to illustrate the electrochemical synthesis-dependent photoelectrochemical properties of the prepared powders. H_2SO_4 was chosen as a supporting electrolyte considering the advantages of acidic media for the proton exchange membrane and the hydrogen evolution process. The anodic current for all samples in the dark is small as expected for semiconductor materials. The anodic current densities under simulated solar light are seen to follow the order WO_3 -OA > WO_3 -SA > WO_3 -NA (Figure 5a). The WO_3 -OA photoanode provided a substantial current density of 0.24 mA/cm^2 at 0.8 V vs. Ag/AgCl in the 0.5 M H_2SO_4 supporting electrolyte, as can be seen from transient photocurrent measurement (Figure 5b).

To evaluate intrinsic potential of PEC system for the electrode/electrolyte interfacial hole injection rate, the OCP of the prepared photoanodes was measured under light irradiation and in the dark. As shown in Figure S7a, $d(\text{OCP})/d(\text{time})$ vs. time curve of WO_3 -OA shows a sharper decay profile that indicates more efficient electron-hole separation. In comparison, $d(\text{OCP})/d(\text{time})$ vs. time profile was recorded for WO_3 -OA sample in the H_2SO_4 /ethanol solution (Figure S7b). The adding of ethanol results in a faster decay profile compared with that in the H_2SO_4 solution due to suppressing the carrier trapping recombination [41]. Thereby, the most crucial thing was to understand how a given photoanode material responds to the different oxygenated species (sacrificial agent). For this reason, chopped-light LSV curves were recorded in aqueous solutions (5 mM) of glycerol, ethylene glycol, glucose, and ethanol (Figure 5c).

Adding of all sacrificial agents results in the extensive current increase under light irradiation. The highest value was obtained in the presence of ethanol. Raptis et al. [6] also observed the highest current in the presence of ethanol using WO_3 photoanodes. However simple alcohols such as ethanol are not ideal biomass-derived feedstocks for PEC reforming. In Figure 5e, the increase in photocurrent for sacrificial agent solution is provided. This enhancement can determine the selectivity towards photoelectrochemical reforming of organic compounds [42]. Excluding glycerol, increases in photocurrent were found to vary between 63 and 87%. Thereby, glucose as a biomass-derived feedstock can be oxidized

at WO_3 photoanodes synthesized under pulse alternating current with current densities comparable to simple alcohols. The phenomenon of significant photocurrent enhancement can be attributed to the so-called current doubling effect at WO_3 photoelectrodes. It can be observed when two electrons are produced in the presence of semiconductor nanoparticles for one photon absorbed. In the case of ethanol, the following reactions (6) and (7) may occur [43]:



The applied bias photon-to-current efficiency (ABPE) is then carried out to quantitatively evaluate the performance of the electrodes (Figure S8). The maximum ABPE was calculated to be 0.2% at 0.8 V vs. RHE in the presence of H_2SO_4 /ethanol solution.

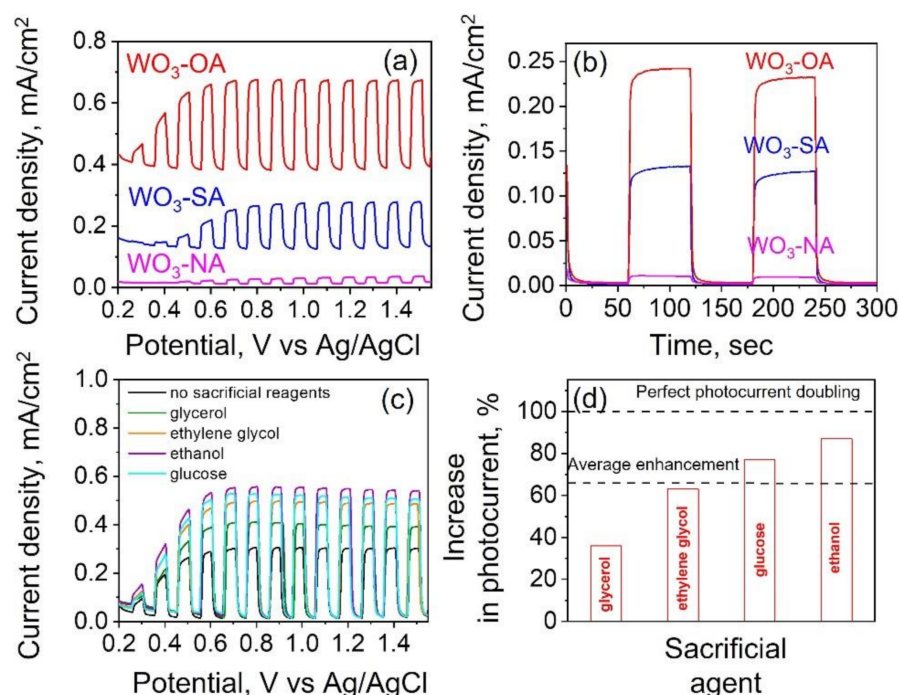


Figure 5. LSV curves (a) and transient photocurrent response at 0.8 V vs. Ag/AgCl (b) under chopped solar illumination in 0.5 M H_2SO_4 ; LSV curves (c) and increase in photocurrent (d) for WO_3 -OA sample in 5 mM sacrificial agent solution compared with 0.5 M H_2SO_4 solution.

For a better understanding of differences in photoelectrochemical performance of WO_3 , the electrochemical active surface area (ECSA) was estimated from the electrochemical double layer capacitance (C_{dl}) measurements. The non-Faradaic region was typically a 0.1 V window about OCP, and all measured currents in this region were assumed to be due to double-layer charging [44,45]. Figure S9a–c show the CV of WO_3 samples prepared in different electrolytes. The linear slope of capacitive current versus scan rate could be used to calculate the C_{dl} of the samples. The large slope represents the large ECSA. C_{dl} values followed the order $\text{WO}_3\text{-NA} < \text{WO}_3\text{-SA} < \text{WO}_3\text{-OA}$ (Figure S9d) which are in accordance with the observed photoelectrochemical activity. The increased C_{dl} value indicated an enhanced electrochemically active surface area, which is beneficial for photoelectrochemical performance.

Electrochemical impedance spectroscopy (EIS) studies were carried out to investigate the charge transport behavior of the photoanode materials prepared in different electrolytes. Figure S10 presents the Nyquist impedance plots of the WO_3 -OA, WO_3 -SA, and WO_3 -NA samples under illumination. The impedance spectra can be divided into a semicircle arc in the high frequency region and a straight line in the low frequency region. Equivalent circuit

model was proposed to illustrate corresponding electrochemical system. R_s characterizes the ohmic resistance of electrolyte solution and FTO glass resistance. R_s was found to be approximately the same for all samples due to the similar experimental conditions (electrolyte and photoelectrochemical cell) [46]. CPE_{dl} represents a capacitance of double layer. R_{ct} is the transfer charge resistance at the electrode/electrolyte interface. Decrease in R_{ct} value indicates a lower resistance due to more efficient charge transfer and separation of photo generated electron–hole pairs. The estimated values of R_s and R_{ct} are 33.0, 32.6, 31.4, and 55.1, 69.3, 84.2 Ω , respectively, for WO_3 -OA, WO_3 -SA, and WO_3 -NA. Z_W is the Warburg impedance which describes the diffusion transport in the electrolyte solution. In addition, the straight line obtained in the low frequency region is vertically more linear for WO_3 -OA compared to other samples, indicating that the sample prepared in oxalic acid has a lower diffusion resistance.

4. Conclusions

In summary, we have described a simple, industrially applicable, and environmentally friendly synthesis of WO_3 nanopowders by electrochemical oxidation of tungsten under pulse alternating current in acidic electrolytes. Investigation of electrolyte composition (oxalic, sulfuric, and nitric acid) was performed to establish a relation between the characteristics of the obtained materials and their photoelectrochemical performance. We demonstrated that using nitric acid as an electrolyte results in formation of the mixture of plates with a length of 400–600 nm and nanoparticles with a side length of approximately 30 nm. Irregular and round-shaped nanoparticles with a side length of 10–30 nm were obtained in sulfuric and oxalic acids, respectively. The high tungsten oxidation rate of up to $0.31 \text{ g cm}^{-2} \text{ h}^{-1}$ was achieved in the oxalic acid solution. The maximum photocurrent density was found to be $\sim 0.25 \text{ mA/cm}^2$ and 0.55 mA/cm^2 at 0.8 V vs. Ag/AgCl in H_2SO_4 and H_2SO_4 /ethanol solution, respectively. Glucose is found to be a biomass-derived feedstock which can be oxidized at electrochemically synthesized WO_3 photoanodes with photocurrents comparable to ethanol. The enhanced PEC activity of tungsten oxide prepared in oxalic acid could be attributed to the optimal morphological, electronic, and charge-transfer properties. This work demonstrates the promise of gram-scale electrosynthesis in oxalic acid as an efficient and sustainable method to produce WO_3 nanopowders for photoelectrochemical applications.

Supplementary Materials: The following supporting information can be downloaded at: <https://www.mdpi.com/article/10.3390/chemengineering6020031/s1>, Table S1: Fitting data of XRD patterns of WO_3 samples using MAUD software; Figure S1: Lorentzian curve fitting for Raman spectra of WO_3 -OA (a), WO_3 -SA (b) and WO_3 -NA (c) samples; Figure S2: Nitrogen adsorption–desorption isotherms of WO_3 -OA (a), WO_3 -SA (b) and WO_3 -NA (c) samples; Figure S3: Effect of electrolyte concentration on tungsten electrochemical oxidation rate using different electrolytes; Figure S4: XRD patterns of the as-prepared powders by electrochemical oxidation of tungsten under pulse alternating current in comparison with the reference pattern of tungstite $WO_3 \cdot H_2O$; Figure S5: SEM image of the film structure obtained on tungsten electrode during electrochemical oxidation of W in oxalic acid under of pulse alternating current; Figure S6: OCP decay derivative of $d(OCP)/d(\text{Time})$ vs. time curves of WO_3 samples in H_2SO_4 (a) and in H_2SO_4 /ethanol (b) solution; Figure S8: Applied bias photon-to-current efficiency (ABPE, %) as a function of applied potential for WO_3 -OA sample; Figure S9: CVs at different scan rates in the potential range of 0.52–0.72 V vs. the RHE (nonfaradaic region) in 0.5 M H_2SO_4 solution of (a) WO_3 -OA, (b) WO_3 -SA and (c) WO_3 -NA; (d) Capacitive currents measured at 0.62 V vs. the RHE as a function of scan rates; Figure S10: Nyquist plots of a WO_3 samples obtained in different electrolytes. The inset shows the equivalent circuit used for fitting the data with the resistances R_s and R_{ct} , the Warburg impedance Z_w , the constant phase element CPE_{dl} and the capacitance C_1 .

Author Contributions: Conceptualization, A.U.; Investigation, A.T., M.G., A.Y., D.Z., V.B. and V.K.; Methodology, A.U.; Writing—Original draft, A.T. and A.U.; Writing—Review & editing, A.U. All authors have read and agreed to the published version of the manuscript.

Funding: This research was funded by RUSSIAN SCIENCE FOUNDATION, grant number 21-79-00079.

Institutional Review Board Statement: Not applicable.

Informed Consent Statement: Not applicable.

Data Availability Statement: Not applicable.

Acknowledgments: The TEM study was carried out on the equipment of the Center Collective Use “Materials Science and Metallurgy” which was purchased with the financial support of the Russian Federation represented by the Ministry of Education and Science (No. 075-15-2021-696). The XPS study was conducted using the equipment of the Center of Collective Use “National Center of Catalyst Research”. The authors also thank the Shared Research Center “Nanotechnologies” of Platov South-Russian State Polytechnic University (NPI) for XRD investigations.

Conflicts of Interest: The authors declare no conflict of interest.

References

1. Momeni, M.M.; Akbarnia, M.; Ghayeb, Y. Preparation of S–W-codoped TiO₂ nanotubes and effect of various hole scavengers on their photoelectrochemical activity: Alcohol series. *Int. J. Hydrogen Energy* **2020**, *45*, 33552–33562. [[CrossRef](#)]
2. Kurenkova, A.Y.; Markovskaya, D.V.; Gerasimov, E.Y.; Prosvirin, I.P.; Cherepanova, S.V.; Kozlova, E.A. New insights into the mechanism of photocatalytic hydrogen evolution from aqueous solutions of saccharides over CdS-based photocatalysts under visible light. *Int. J. Hydrogen Energy* **2020**, *45*, 30165–30177. [[CrossRef](#)]
3. Markovskaya, D.V.; Zhurenok, A.V.; Kurenkova, A.Y.; Kremneva, A.M.; Saraev, A.A.; Zharkov, S.M.; Kozlova, E.A.; Kaichev, V.V. New titania-based photocatalysts for hydrogen production from aqueous-alcoholic solutions of methylene blue. *RSC Adv.* **2020**, *10*, 34137–34148. [[CrossRef](#)]
4. López, C.R.; Melián, E.P.; Ortega Méndez, J.A.; Santiago, D.E.; Doña Rodríguez, J.M.; González Díaz, O. Comparative study of alcohols as sacrificial agents in H₂ production by heterogeneous photocatalysis using Pt/TiO₂ catalysts. *J. Photochem. Photobiol. A Chem.* **2015**, *312*, 45–54. [[CrossRef](#)]
5. Liu, X.; Wei, W.; Ni, B.-J. Photocatalytic and Photoelectrochemical Reforming of Biomass. In *Solar-to-Chemical Conversion*; WILEY-VCH: Weinheim, Germany, 2021; pp. 389–417.
6. Raptis, D.; Dracopoulos, V.; Lianos, P. Renewable energy production by photoelectrochemical oxidation of organic wastes using WO₃ photoanodes. *J. Hazard. Mater.* **2017**, *333*, 259–264. [[CrossRef](#)]
7. Wang, Y.; Zhang, J.; Balogun, M.S.; Tong, Y.; Huang, Y. Oxygen Vacancy-Based Metal Oxides Photoanodes in Photoelectrochemical Water Splitting. *Mater. Today Sustain.* **2022**, *18*, 100118. [[CrossRef](#)]
8. Shandilya, P.; Sambyal, S.; Sharma, R.; Mandyal, P.; Fang, B. Properties, optimized morphologies, and advanced strategies for photocatalytic applications of WO₃ based photocatalysts. *J. Hazard. Mater.* **2022**, *428*, 128218. [[CrossRef](#)]
9. Zhang, J.; Salles, I.; Pering, S.; Cameron, P.J.; Mattia, D.; Eslava, S. Nanostructured WO₃ photoanodes for efficient water splitting via anodisation in citric acid. *RSC Adv.* **2017**, *7*, 35221–35227. [[CrossRef](#)]
10. Shabdan, Y.; Markhabayeva, A.; Bakranov, N.; Nuraje, N. Photoactive Tungsten-Oxide Nanomaterials for Water-Splitting. *Nanomaterials* **2020**, *10*, 1871. [[CrossRef](#)]
11. Dutta, V.; Sharma, S.; Raizada, P.; Thakur, V.K.; Khan, A.A.P.; Saini, V.; Asiri, A.M.; Singh, P. An overview on WO₃ based photocatalyst for environmental remediation. *J. Environ. Chem. Eng.* **2021**, *9*, 105018. [[CrossRef](#)]
12. Izzì, M.; Sportelli, M.C.; Ditaranto, N.; Picca, R.A.; Innocenti, M.; Sabbatini, L.; Cioffi, N. Pros and Cons of Sacrificial Anode Electrolysis for the Preparation of Transition Metal Colloids: A Review. *ChemElectroChem* **2020**, *7*, 386–394. [[CrossRef](#)]
13. Gao, D.; Li, H.; Wei, P.; Wang, Y.; Wang, G.; Bao, X. Electrochemical synthesis of catalytic materials for energy catalysis. *Chin. J. Catal.* **2022**, *43*, 1001–1016. [[CrossRef](#)]
14. Zhang, T.; Paulose, M.; Neupane, R.; Schaffer, L.A.; Rana, D.B.; Su, J.; Guo, L.; Varghese, O.K. Nanoporous WO₃ films synthesized by tuning anodization conditions for photoelectrochemical water oxidation. *Sol. Energy Mater. Sol. Cells* **2020**, *209*, 110472. [[CrossRef](#)]
15. Fernández-Domene, R.M.; Sánchez-Tovar, R.; Lucas-Granados, B.; Roselló-Márquez, G.; García-Antón, J. A simple method to fabricate high-performance nanostructured WO₃ photocatalysts with adjusted morphology in the presence of complexing agents. *Mater. Des.* **2017**, *116*, 160–170. [[CrossRef](#)]
16. Wu, S.; Li, Y.; Chen, X.; Liu, J.; Gao, J.; Li, G. Fabrication of WO₃·2H₂O nanoplatelet powder by breakdown anodization. *Electrochem. Commun.* **2019**, *104*, 106479. [[CrossRef](#)]
17. Ulyankina, A.; Molodtsova, T.; Gorshenkov, M.; Leontyev, I.; Zhigunov, D.; Konstantinova, E.; Lastovina, T.; Tolasz, J.; Henych, J.; Licciardello, N.; et al. Photocatalytic degradation of ciprofloxacin in water at nano-ZnO prepared by pulse alternating current electrochemical synthesis. *J. Water Process Eng.* **2021**, *40*, 101809. [[CrossRef](#)]

18. Ulyankina, A.; Leontyev, I.; Maslova, O.; Allix, M.; Rakhmatullin, A.; Nevzorova, N.; Valeev, R.; Yalovega, G.; Smirnova, N. Copper oxides for energy storage application: Novel pulse alternating current synthesis. *Mater. Sci. Semicond. Process.* **2018**, *73*, 111–116. [[CrossRef](#)]
19. Sadek, A.Z.; Zheng, H.; Breedon, M.; Bansal, V.; Bhargava, S.K.; Latham, K.; Zhu, J.; Yu, L.; Hu, Z.; Spizzirri, P.G.; et al. High-Temperature Anodized WO₃ Nanoplatelet Films for Photosensitive Devices. *Langmuir* **2009**, *25*, 9545–9551. [[CrossRef](#)]
20. Xie, Y.P.; Liu, G.; Yin, L.; Cheng, H.-M. Crystal facet-dependent photocatalytic oxidation and reduction reactivity of monoclinic WO₃ for solar energy conversion. *J. Mater. Chem.* **2012**, *22*, 6746–6751. [[CrossRef](#)]
21. Pokhrel, S.; Birkenstock, J.; Dianat, A.; Zimmermann, J.; Schowalter, M.; Rosenauer, A.; Ciacchi, L.C.; Mädler, L. In situ high temperature X-ray diffraction, transmission electron microscopy and theoretical modeling for the formation of WO₃ crystallites. *CrystEngComm* **2015**, *17*, 6985–6998. [[CrossRef](#)]
22. Desseigne, M.; Dirany, N.; Chevallier, V.; Arab, M. Shape dependence of photosensitive properties of WO₃ oxide for photocatalysis under solar light irradiation. *Appl. Surf. Sci.* **2019**, *483*, 313–323. [[CrossRef](#)]
23. Efkeri, H.İ.; Gümrukçü, A.E.; Özen, Y.; Kınacı, B.; Aydın, S.Ş.; Ates, H.; Özçelik, S. Investigation of the effect of annealing on the structural, morphological and optical properties of RF sputtered WO₃ nanostructure. *Phys. B Condens. Matter* **2021**, *622*, 413350. [[CrossRef](#)]
24. Li, Y.; Tang, Z.; Zhang, J.; Zhang, Z. Defect Engineering of Air-Treated WO₃ and Its Enhanced Visible-Light-Driven Photocatalytic and Electrochemical Performance. *J. Phys. Chem. C* **2016**, *120*, 9750–9763. [[CrossRef](#)]
25. Jin, B.; Wang, J.; Xu, F.; Li, D.; Men, Y. Hierarchical hollow WO₃ microspheres with tailored surface oxygen vacancies for boosting photocatalytic selective conversion of biomass-derived alcohols. *Appl. Surf. Sci.* **2021**, *547*, 149239. [[CrossRef](#)]
26. Vargas-Consuelos, C.I.; Seo, K.; Camacho-López, M.; Graeve, O.A. Correlation between Particle Size and Raman Vibrations in WO₃ Powders. *J. Phys. Chem. C* **2014**, *118*, 9531–9537. [[CrossRef](#)]
27. Li, Y.H.; Liu, P.F.; Pan, L.F.; Wang, H.F.; Yang, Z.Z.; Zheng, L.R.; Hu, P.; Zhao, H.J.; Gu, L.; Yang, H.G. Local atomic structure modulations activate metal oxide as electrocatalyst for hydrogen evolution in acidic water. *Nat. Commun.* **2015**, *6*, 8064. [[CrossRef](#)]
28. Abbaspoor, M.; Aliannezhadi, M.; Tehrani, F.S. Effect of solution pH on as-synthesized and calcined WO₃ nanoparticles synthesized using sol-gel method. *Opt. Mater.* **2021**, *121*, 111552. [[CrossRef](#)]
29. Colton, R.J.; Rabalais, J.W. Electronic structure of tungsten and some of its borides, carbides, nitrides, and oxides by x-ray electron spectroscopy. *Inorg. Chem.* **1976**, *15*, 236–238. [[CrossRef](#)]
30. Fleisch, T.H.; Mains, G.J. An XPS study of the UV reduction and photochromism of MoO₃ and WO₃. *J. Chem. Phys.* **1982**, *76*, 780–786. [[CrossRef](#)]
31. Ramana, C.V.; Vemuri, R.S.; Kaichev, V.V.; Kochubey, V.A.; Saraev, A.A.; Atuchin, V.V. X-ray Photoelectron Spectroscopy Depth Profiling of La₂O₃/Si Thin Films Deposited by Reactive Magnetron Sputtering. *ACS Appl. Mater. Interfaces* **2011**, *3*, 4370–4373. [[CrossRef](#)]
32. Al-Kandari, H.; Al-Kharafi, F.; Al-Awadi, N.; El-Dusouqui, O.M.; Katrib, A. Surface electronic structure–catalytic activity relationship of partially reduced WO₃ bulk or deposited on TiO₂. *J. Electron Spectrosc. Relat. Phenom.* **2006**, *151*, 128–134. [[CrossRef](#)]
33. Cheshme Khavar, A.H.; Moussavi, G.; Yaghmaeian, K.; Mahjoub, A.R.; Khedri, N.; Dusek, M.; Vaclavu, T.; Hosseini, M. A new Ru(ii) polypyridyl complex as an efficient photosensitizer for enhancing the visible-light-driven photocatalytic activity of a TiO₂/reduced graphene oxide nanocomposite for the degradation of atrazine: DFT and mechanism insights. *RSC Adv.* **2020**, *10*, 22500–22514. [[CrossRef](#)]
34. Liu, Q.; Wang, F.; Lin, H.; Xie, Y.; Tong, N.; Lin, J.; Zhang, X.; Zhang, Z.; Wang, X. Surface oxygen vacancy and defect engineering of WO₃ for improved visible light photocatalytic performance. *Catal. Sci. Technol.* **2018**, *8*, 4399–4406. [[CrossRef](#)]
35. Wang, L.; Wang, Y.; Cheng, Y.; Liu, Z.; Guo, Q.; Ha, M.N.; Zhao, Z. Hydrogen-treated mesoporous WO₃ as a reducing agent of CO₂ to fuels (CH₄ and CH₃OH) with enhanced photothermal catalytic performance. *J. Mater. Chem. A* **2016**, *4*, 5314–5322. [[CrossRef](#)]
36. Anik, M.; Cansizoglu, T. Dissolution kinetics of WO₃ in acidic solutions. *J. Appl. Electrochem.* **2006**, *36*, 603–608. [[CrossRef](#)]
37. Fernández-Domene, R.M.; Sánchez-Tovar, R.; Segura-Sanchís, E.; García-Antón, J. Novel tree-like WO₃ nanoplatelets with very high surface area synthesized by anodization under controlled hydrodynamic conditions. *Chem. Eng. J.* **2016**, *286*, 59–67. [[CrossRef](#)]
38. Seifollahi Bazarjani, M.; Hojamberdiev, M.; Morita, K.; Zhu, G.; Cherkashinin, G.; Fasel, C.; Herrmann, T.; Breitzke, H.; Gurlo, A.; Riedel, R. Visible Light Photocatalysis with c-WO_{3-x}/WO₃ × H₂O Nanoheterostructures In Situ Formed in Mesoporous Polycarbosilane-Siloxane Polymer. *J. Am. Chem. Soc.* **2013**, *135*, 4467–4475. [[CrossRef](#)]
39. Pham, N.L.; Luu, T.L.A.; Nguyen, H.L.; Nguyen, C.T. Effects of acidity on the formation and adsorption activity of tungsten oxide nanostructures prepared via the acid precipitation method. *Mater. Chem. Phys.* **2021**, *272*, 125014. [[CrossRef](#)]
40. Cherevko, S.; Kulyk, N.; Chung, C.-H. Pulse-reverse electrodeposition for mesoporous metal films: Combination of hydrogen evolution assisted deposition and electrochemical dealloying. *Nanoscale* **2012**, *4*, 568–575. [[CrossRef](#)]
41. Tang, R.; Wang, L.; Zhang, Z.; Yang, W.; Xu, H.; Kheradmand, A.; Jiang, Y.; Zheng, R.; Huang, J. Fabrication of MOFs' derivatives assisted perovskite nanocrystal on TiO₂ photoanode for photoelectrochemical glycerol oxidation with simultaneous hydrogen production. *Appl. Catal. B Environ.* **2021**, *296*, 120382. [[CrossRef](#)]

42. Esposito, D.V.; Forest, R.V.; Chang, Y.; Gaillard, N.; McCandless, B.E.; Hou, S.; Lee, K.H.; Birkmire, R.W.; Chen, J.G. Photoelectrochemical reforming of glucose for hydrogen production using a WO₃-based tandem cell device. *Energy Environ. Sci.* **2012**, *5*, 9091–9099. [[CrossRef](#)]
43. Kalamaras, E.; Lianos, P. Current Doubling effect revisited: Current multiplication in a PhotoFuelCell. *J. Electroanal. Chem.* **2015**, *751*, 37–42. [[CrossRef](#)]
44. McCrory, C.C.L.; Jung, S.; Peters, J.C.; Jaramillo, T.F. Benchmarking Heterogeneous Electrocatalysts for the Oxygen Evolution Reaction. *J. Am. Chem. Soc.* **2013**, *135*, 16977–16987. [[CrossRef](#)] [[PubMed](#)]
45. Nayak, A.K.; Verma, M.; Sohn, Y.; Deshpande, P.A.; Pradhan, D. Highly Active Tungsten Oxide Nanoplate Electrocatalysts for the Hydrogen Evolution Reaction in Acidic and Near Neutral Electrolytes. *ACS Omega* **2017**, *2*, 7039–7047. [[CrossRef](#)]
46. Yoo, S.J.; Lim, J.W.; Sung, Y.-E.; Jung, Y.H.; Choi, H.G.; Kim, D.K. Fast switchable electrochromic properties of tungsten oxide nanowire bundles. *Appl. Phys. Lett.* **2007**, *90*, 173126. [[CrossRef](#)]